15TH IEA HEAT PUMP CONFERENCE
MAY 26–29, 2026 | HOFBURG VIENNA 2026
DECARBONISATION THROUGH INNOVATION

Modeling and Experimental Validation of a Multifluid Brazed Plate Heat Exchanger for Multi-Circuit Heat Pump Applications

Ganesh B. Venkatesan*, Riley B. Barta

Ray W. Herrick Laboratories, School of Mechanical Engineering, Purdue University, West Lafayette, IN, 47901, USA

Abstract

Multi-fluid plate heat exchangers (PHE) enable compact, multifunctional heat management for thermal systems that must dynamically integrate with multiple heat sinks or sources, decarbonized examples of which are solar, air, water and ground-source heat reservoirs, among others. This paper presents a modeling and validation framework for a multifluid brazed PHE designed for a multi-circuit heat pump (HP) system coupled to a shared water loop. A steady-state finite-volume thermal-hydraulic model is developed using Python and a transient dynamic model is implemented in Modelica using the Dymola simulation environment to capture variable-temperature, multi-source and multi-sink operation. The models are validated against experimental data from a dual-circuit HP using R32 as the refrigerant, for water cooling applications. This modelling framework can be extended to natural refrigerants and next-generation low-global warming potential (GWP) refrigerant mixtures, providing a robust foundation for future design, optimization, and control of advanced thermal systems integrating alternative energy sources, waste heat recovery and thermal energy storage.

© HPC2026.
Selection and/or peer-review under the responsibility of the organizers of the 15th IEA Heat Pump Conference 2026.

Keywords: Plate heat exchanger; Multi-source heat pump; Decarbonization; Energy efficiency

1. Introduction

Heat pumps (HPs) offer a central pathway to reduce emissions and achieve climate neutrality. However, their efficiency remains strongly dependent on the source temperature, with air-source HPs penalized by low-ambient performance limits and defrost losses [1,2,3] in contrast to ground-source systems that rely on stable subsurface temperatures, but require expensive borefield installations [4]. To address the source temperature limitations of single source heat pumps, multi-source heat pump (MSHP) systems combine complementary heat sources such as air, ground, water, solar energy and waste heat. By dynamically allocating heat loads across sources, MSHPs improve seasonal COP, enhance source stability, reduce defrost losses and reduce total life cycle costs [5,6].

Realizing the full potential of MSHPs requires components capable of efficiently coupling multiple refrigeration circuits with a secondary (hydronic or equivalent) load. Brazed plate heat exchangers (PHEs) have long been favored in heat pump applications for their compactness, high thermal efficiency, and low refrigerant charge. As MSHP architectures increasingly demand the integration of multiple refrigerant circuits within a shared secondary loop, conventional single-circuit PHEs become insufficient to provide the required operational flexibility. In this context, dual-circuit, six-port PHEs emerge as a natural extension of traditional PHE designs, enabling (i) simultaneous or independent operation of two refrigerant circuits, (ii) staging and redundancy, and (iii) source switching or parallel operation of the refrigeration circuits while maintaining a

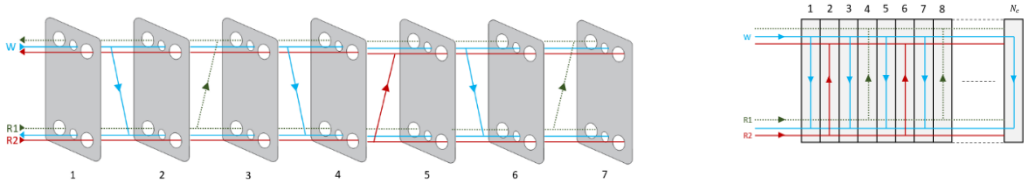
* Corresponding author. Tel.: +1 765-543-8688
E-mail address: gbramman@purdue.edu

single hydronic interface. Manufacturers have documented such designs and their advantages [7,8]. Thermal design theory for three-fluid heat exchangers using the effectiveness–NTU approach, providing a basis for rating/sizing beyond conventional two-stream formulations, was presented in [9]. A mathematical model in algorithm form for steady state simulations of PHE with generalized configurations was developed in [10]. The study investigated the influence of the PHE configuration on the heat exchanger performance, but it verifies only two fluids. A general flexible modelling framework for multi stream heat exchangers such as tube in-shell, plate, plate-fin heat exchangers by defining a number of building blocks like fluid and solid elements that are connected by heat nodes through a surface and simulated more than 1000 cases using multi stream tube and shell heat exchanger was introduced in [11]. Of particular interest was a new model for PHEs created by [12] to study the steady state thermal performance of generalized flow configurations for multi fluid, multi stream and multi pass configurations using the concept of concept of Junction-Channel Connectivity Matrix. Despite growing industrial adoption, physics bases steady state and transient models for dual-circuit, six port PHEs remain scarce in the open literature, particularly for MSHP applications. This study develops and experimentally validates a steady-state finite volume model in Python and a transient Modelica model in Dymola by extending the TIL Suite [13] four port PHE to a six-port configuration, The system is evaluated using two air cooled vapor compression circuits to ensure well-defined and relevant MSHP conditions. The validated models can be used to quantify the impacts of circuit staging, redundancy, and load redistribution on capacity, COP and thermal balance demonstrating the efficiency and flexibility enabled by six-port PHEs.

2. Numerical Methodology

2.1. Six port plate heat exchanger

Six port PHEs employ three distinct loops in which three fluids can be used to transfer heat simultaneously. The six port PHE configuration used in this study is shown in Figure 1(a), where refrigerant circuit 1 (R1) flows through the left-side ports, refrigerant circuit 2 (R2) through the right-side ports, and the water circuit through the central ports. The integrated setup reduces thermal losses that can occur when transferring heat across two separate circuits and allows better synchronization of the two refrigerant circuits. In this configuration, the water will be in contact with both the refrigerant circuits across its entire length, except for the first and last channels, enabling more precise control over the heat exchange process. An example of this arrangement with a seven-plate configuration is shown in Figure 1(a) and the channel arrangement for N_c number of channels is shown in Figure 1(b).



(a) (b)

Figure 1. Example flow configuration of a six-port PHE

2.2. Plate heat exchanger geometry

One of the common types of the PHEs is the chevron type PHE. A general chevron PHE is shown in Figure 2(a, b). The geometry of chevron-type plate heat exchangers is characterized by the chevron angle (β), wave length (Λ), and wave amplitude (2â), which collectively influence the thermal-hydraulic performance. Higher β and smaller Λ enhance turbulence and heat transfer but also increase pressure drop. The geometry of the plate heat exchanger used in this study in shown in Table 1.



(a) (b)

Figure 2. Geometric characteristics of the plate found in PHEs

Table 1. Basic geometry values of the plate found in PHEs

Symbol	Description	Unit	Value
W	Width of the plate	mm	289
L	Length of the plate	mm	525
t	Thickness	mm	0.30
k	Thermal conductivity of the plate	W/m-K	15
2â	Plate amplitude	mm	2.21
Λ	Plate wavelength	mm	6.63
β	Plate Inclination angle	degree	25.8
N_p	Number of plates	-	210
d_h	Hydraulic diameter	mm	3.57
Φ	Surface enlargement factor	-	1.237
N_c	Number of flow channels	-	209

where the hydraulic diameter d_h is defined by

$$d_h = \frac{4\hat{a}}{\Phi} \tag{1}$$

the parameter Φ is the ratio of the actual area to the planar area and is defined by

$$\Phi = \frac{1}{6}\left(1 + \sqrt{1 + x^2} + 4\sqrt{1 + x^2/2}\right) \tag{2}$$

and the wavenumber x is given by

$$x = 2\pi\hat{a}/\Lambda \tag{3}$$

Each plate forms a single corrugated flow channel with the adjacent plate, resulting in alternating hot and cold fluid channels throughout the plate pack. The corrugation pattern is assumed to be uniform along the plate length, with a constant chevron angle β and corrugation wavelength Λ. For a PHE of N_p plates, the total number of flow channels is $N_p - 1$, with half of the flow channels are for water and the remaining channels are split between refrigerant circuit 1 and refrigerant circuit 2.

2.3. Heat transfer correlation

The literature on PHEs contains an extensive collection of thermal and transport correlations. Single-phase convection in chevron plates is commonly characterized with established chevron plate correlations such as Martin [14]. In contrast, evaporation lacks a widely-validated PHE-specific correlation because heat transfer depends not only on plate surface structure, heat flux, and mass flux, but also on vapor quality, flow regime, and dry out, among other factors. Experiments consistently indicate that evaporation in PHEs comprises nucleate-boiling and forced-convection contributions: in nucleate-dominated regimes, the heat transfer coefficient (HTC) scales primarily with heat flux. In forced-convection regimes, the HTC scales primarily with vapor quality and mass flux. The dominant mechanism is not uniform across flow regimes. Dominance of both nucleate boiling and forced convection has been reported, and several works support mixed contributions [15]. Experimental validation reported in [16] demonstrated good agreement between measured heat transfer coefficients and predictions from the Cooper pool-boiling correlation [17] over a wide range of heat fluxes in the PHE, concluding that evaporation heat transfer was primarily governed by heat flux than mass flux. Consistent with the finding of that study, the Cooper pool-boiling correlation provides good agreement between experimentally measured and predicted cooling capacities across the investigated operating range, confirming that heat flux driven boiling mechanism is appropriate for the present conditions. Accordingly, the Cooper correlation (4) is adopted in the study to model the two-phase heat transfer coefficient ($\alpha_{2\phi}$)

$$\alpha_{2\phi} = 55\, p^{*(0.12 - 0.2\, log_{10}(rp))} \left(-log_{10}(p^*)\right)^{(-0.55)} q^{(0.67)}\, M^{(-0.5)} \tag{4}$$

The Cooper correlation is consistent with nucleate boiling controlled heat transfer mechanism, because it expresses the two-phase HTC primarily as a function of heat flux (q) and reduced pressure (p^*), without any explicit dependence on mass flux and vapor quality terms which are characteristics of forced convection dominated boiling. The surface roughness term (rp) is set to unity if not known.

The HTC for single phase ($\alpha_{1\phi}$) is given by

$$\alpha_{1\phi} = \frac{k\,Nu}{d_h} \tag{5}$$

$$Nu = c_q Pr^{1/3} (\eta/\eta_w)^{1/6} \left[2H_g\, sin(2\beta)\right]^q \tag{6}$$

3. Steady state numerical modelling

The steady state numerical model of the six-port PHE is developed using a finite volume discretization approach to solve the coupled flow and heat transfer processes within the heat exchanger. The modelling approach builds upon generalized methodologies established for multi-pass, multi-fluid PHEs described in [12] and is specifically extended to capture the unique configuration of the present system. Since the pattern of refrigerant circuit 1, water, then refrigerant circuit 2 is repeated, the entire stack of arrangements is abstracted into a three-channel representative unit, illustrated in Figure 3, where the effective thermal contact areas between water, refrigerant circuit R1, water, and refrigerant circuit R2 across all the channels are summed up and provided as inputs for the thermal resistance network and heat flow calculation. Along the primary flow direction, each channel is subdivided into a series of cells or control volumes using the finite volume method. Each cell represents a discrete element in which conservation of mass, momentum and energy are solved. The modelling framework is based on the following assumptions: 1) Steady-state operation, 2) no heat loss to the surroundings, 3) uniform distribution of flow through all the channels, 4) no heat conduction in the direction of flow, 5) fluid properties are evaluated based on the inlet condition of each segment, 6) phase transition is not considered within a segment, 7) plate surface temperature is assumed to be constant within a segment, 8) heat transfer coefficient is calculated using the fluid properties at the inlet of each segment. For N number of plates, there will be $(N-2)\cdot 2$ number of unknown plate surface temperatures, as shown in Figure 3, that needs to be solved, assuming the PHE is insulated and the first and last plate do not take part in the heat transfer process. Within each cell, the plate surface temperatures are iteratively solved from local energy balances. Each water passage in the center is in thermal contact with two neighboring refrigerant passages, thereby transferring heat simultaneously to refrigerant circuits R1 and R2. During evaporation, the heat flow from the water side to refrigerant circuit R1 is governed by the temperature difference across plate P2, while that to refrigerant circuit R2 is evaluated across plate P3.

Control Volume 1 (CV1) $$\dot{Q}_{R1} = \dot{Q}_{w1} \tag{9}$$

Control Volume 2 (CV2) $$\dot{Q}_{R1} = \dot{Q}_{P2} \tag{10}$$

Control Volume 3 (CV3) $$\dot{Q}_{P3} = \dot{Q}_{R2} \tag{11}$$

Control Volume 4 (CV4) $$\dot{Q}_{R2} = \dot{Q}_{w2} \tag{12}$$

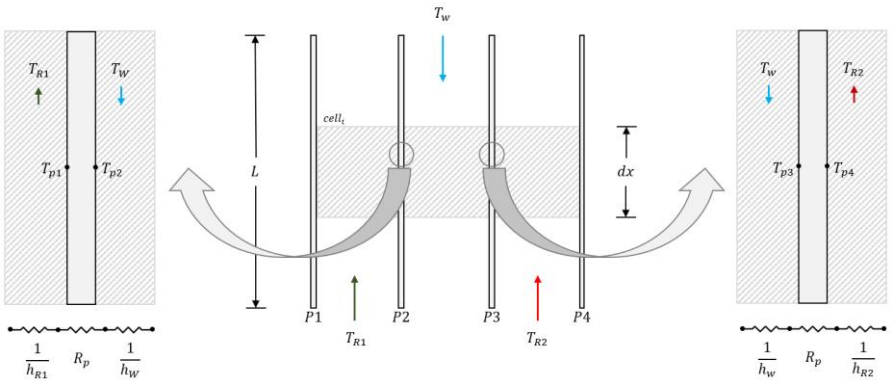


Figure 3. Schematic of a discretized cell in the PHE.

As described in Figure 4, each cell is further divided into four control volumes and the heat balance in each of the control volume is shown below, $\dot{Q}_{R1}$ denotes the convective heat transfer rate from the surface of plate P2 to the adjacent fluid in the region R1, $\dot{Q}_{R2}$ denotes the convective heat transfer rate from the surface of plate P3 to the adjacent fluid in the region R2, $\dot{Q}_{w1}$ denotes the convective heat transfer rate from the surface of plate P2 to the adjacent fluid in the water circuit region, $\dot{Q}_{w2}$ denotes the convective heat transfer rate from the surface of plate P3 to the adjacent fluid in the water circuit region, $\dot{Q}_{P2}$ denotes the conduction heat transfer rate across the plate P2 and $\dot{Q}_{P3}$ denotes the conduction heat conduction rate across the plate P3

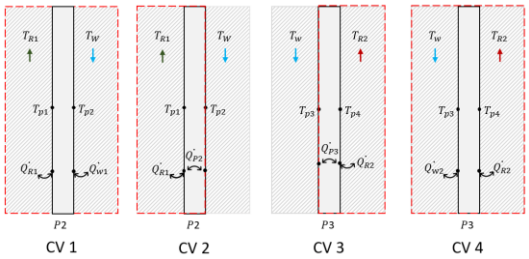


Figure 4. Schematic of the control volumes used in PHE energy balances.

The model is developed for both parallel flow and counter flow configuration. The flow of the code for counter flow configuration is described in the flowchart in Figure 5. Since only the inlet conditions of R1 and R2 are known at length z = 0 in a counter-flow orientation, the procedure begins with an initial guess for the water outlet temperature $T_{w,out,guess}$ at z = 0. The model then evaluates the heat exchanger cell by cell across the length (L) using a spatial index variable z, starting at z = 0 and progressing toward z = L. $T_{w,out,guess}$ serves as a global convergence parameter for the outer iteration loop for the counter flow heat exchanger. The inlet conditions for cell 1 at z = 0, including inlet refrigerant pressure, specific enthalpy and mass flow rate, as well as water inlet temperature and mass flow rate, are specified for the cell.

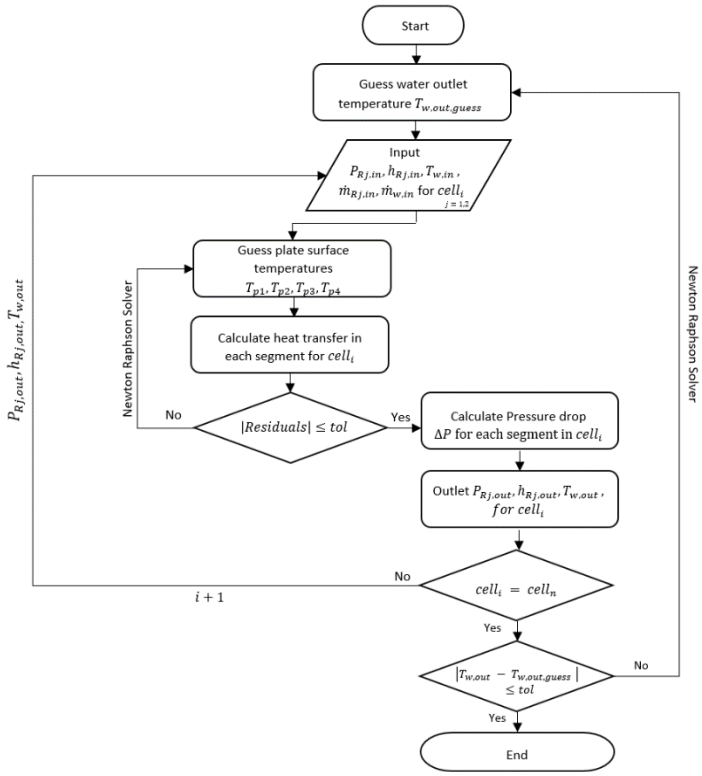


Figure 5. Flow chart of the counter flow steady state numerical modelling code.

Within each cell, plate surface temperatures (T_{Pi}) are initially guessed and local heat transfer rates are computed for each segment using energy balances derived from the finite volume formulation and the plate surface temperatures are iterated until the residuals of the energy balance equations for all control volumes are less than the specified convergence tolerance ($tol = 1 \cdot 10^{-3}$), which constitutes the inner iteration loop. Once the energy balance is satisfied, the pressure drop across the cell is computed using pressure drop correlations.

The resulting outlet conditions of each cell are then propagated to calculate the new thermo-physical properties at the inlet conditions to the subsequent cell. This sequential marching continues until all the cells along the heat exchanger length have been solved. Upon reaching the final cell, the calculated outlet water temperature $T_{w,out}$ is compared with the initial guess value. The outer iteration loop updates the guessed outlet temperature, and the entire calculation is repeated until the difference satisfies the global convergence criterion ($tol = 1 \cdot 10^{-2}$).

4. Transient simulation

One of the major advantages of the multi-fluid heat exchanger is to enable hybrid operation by coupling a stable source or sink with an intermittent, time dependent source, such as a ground loop, solar, thermal energy storage, or other thermal system. Transient simulation is therefore necessary to capture heat exchanger performance under dynamic conditions. Operationally, this paper extends the TIL Suite four-port PHE to a six-port PHE by adding a second refrigerant-side thermal interface to the same central water wall, creating two independent refrigerant paths that exchange heat simultaneously with the single water channel, as shown in Figure 6.

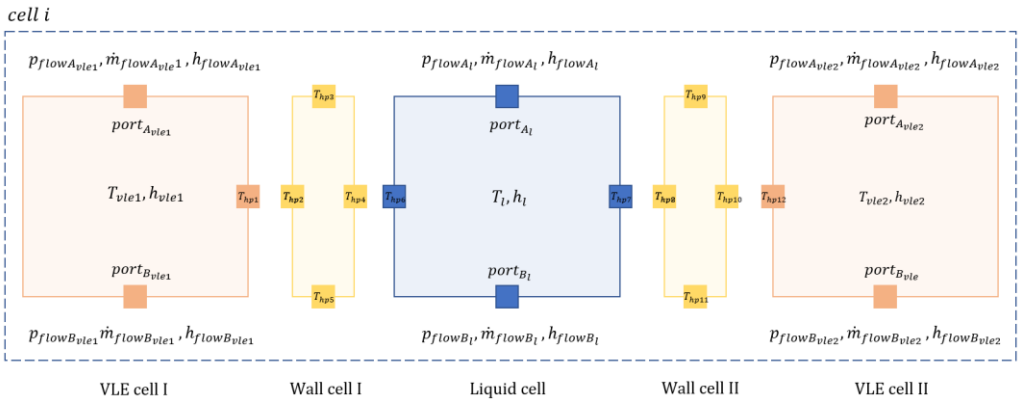


Figure 6. Each cell in the PHE path for the presented dynamic model.

Similar to the strategy explained in the steady state modelling section, each channel is spatially discretized in Dymola into finite volume segments. The central plate is modeled as a lumped thermal mass with through-thickness conduction and heat capacity. Fluid cells which, in this case, consist of water and vapor-liquid equilibrium (VLE) refrigerants, have two fluid connectors ($port_A$, $port_B$) that associated with a pressure, mass flow, and specific enthalpy, as well as wall heat ports (T_{hp}) that exchange only heat flow. Per segment, the heat transfer rate across interfaces is obtained from two convective films, being the water-side and the refrigerant-side, in series with plate conduction to form the local overall heat transfer coefficient U. Modelica connector laws enforce energy, mass and momentum conservation, such that the same heat rate that leaves the water cell enters the corresponding refrigerant cell, thus neglecting stray heat loss. The governing equations are adopted from the VLE and liquid cell formulations provided in the TIL Suite library. In the VLE fluid cell, the transient energy balance (13) accounts for convective enthalpy transport through the inlet and outlet ports, interfacial heat transfer with the wall ($\dot{Q}_{flow}$) and pressure work associated with time-dependent pressure variations, the mass balance (14) equation governs the evolution of mixture composition due to mass exchange across the ports under the assumption of a perfectly mixed control volume, while the momentum balance (15) is enforced though an algebraic pressure drop relation between the inlet and outlet ports.

$$\frac{dh}{dt} = \frac{\dot{m}_{flowA} \cdot (h_{flowA} - h_{vle}) + \dot{m}_{flowB} \cdot (h_{flowB} - h_{vle}) + \dot{Q}_{flow} + v.(dp/dt)}{m_{vle}} \tag{13}$$

$$\frac{d\xi}{dt} = \frac{\dot{m}_{flowA} \cdot (\xi_{flowA} - \xi_{vle}) + \dot{m}_{flowB} \cdot (\xi_{flowB} - \xi_{vle})}{m_{vle}} \tag{14}$$

$$p_A - p_B = \Delta p \tag{15}$$

The liquid cell follows a similar formulation, solving a transient mass balance (16) that accounts for thermal expansion, an energy balance (17) with temperature as the state variable, and with the interfacial heat transfer defined by the convective heat transfer relation (18) and momentum balance (19). Collectively, these equations form a coupled differential- algebraic system that captures the dynamic interaction between heat transfer, phase change and fluid transport within each heat exchanger segment.

$$\dot{m}_{flowA} + \dot{m}_{flowB} = -\beta \cdot \rho_l \left(\frac{dT_l}{dt}\right) \cdot v \tag{16}$$

$$\frac{dT_l}{dt} = \frac{\dot{m}_{flowA} \cdot \left(h_{flowA} - h_l\right) + \dot{m}_{flowB} \cdot \left(h_{flowB} - h_l\right) + \dot{Q}_{flow}}{c_p \cdot m_l} \tag{17}$$

$$\dot{Q}_{flow} = \alpha \,.\, A \,.\, \left(T_{hp} - T_l\right) \tag{18}$$

$$p_A - p_B = \Delta p \tag{19}$$

At each solver step, the system of differential algebraic equations (DAE) is advanced with an implicit solver based on Differential Algebraic System Solver (DASSL) algorithm [18]. The DASSL algorithm predicts the first-time derivatives of state variables using backward differentiation formulas (BDF) as part of its solution strategy, which is crucial for maintaining the numerical stability and achieving efficient convergence. This numerical foundation allows the solver to (i) update U from the film coefficients and plate conduction, (ii) attain an energy balance between the interacting control volumes, (iii) perform VLE flash calculations to update mass-based quality, densities, and specific enthalpies, and (iv) resolve momentum balances to obtain segment-wise pressure drops with the appropriate phase, being single-phase on the water-side and two-phase on the refrigerant-side. Steady state is reached when all state derivatives with respect to time vanish and the segment residuals close. In transients, the plate heat capacity and fluid capacitances mediate the coupling between water-side perturbations and the refrigerant evaporation or condensation response. Mixing in headers and maldistribution are excluded in this model and the applied refrigerant heat transfer correlations for single phase and two phase are same as were used in the steady state model.

5. Experimental Validation

The experimental validation was conducted at Daikin Applied Psychrometrics Laboratories. For this purpose, a six-port PHE was integrated into a dual air source vapor-compression refrigeration system, as illustrated in Figure 7. Refrigerant circuit 1 consist of two compressors with a swept volume of 407.2 cm^3/rev each, paired with two V-shaped condenser coils, while refrigerant circuit 2 employed one compressor with a swept volume of 170.3 cm^3/rev and another compressor with a swept volume of 227.6 cm^3/rev in parallel, connected with a single V-shaped condenser coil. Both refrigerant circuits were instrumented with pressure and temperature sensors at the inlet and outlet of all major components. The specifications of the pyschrometrics chamber are mentioned in Table 2. To capture operating conditions of the PHE, pressure transducers and temperature sensors were installed at the inlet and outlet of both the refrigerant and water circuits. The measurement instrument specifications and accuracy are tabulated in Table 3. The refrigerant mass flow rate was determined using compressor performance polynomials and cross-verified through an overall energy balance of the system. The water-side mass flow rate was measured directly using a calibrated Coriolis flow meter. This ensured accurate characterization of the energy balance across the PHE.

Table 2. Psychrometric laboratory specifications

Parameters	Unit	Range
Psychrometric chamber capacity	kW	808
Dry bulb temperature	°C	-26 to 60
Air flow	CFM	200,000
Water flow rate	GPM	140 - 600
Evaporator leaving water temperature range	°C	3.3 to 35
Voltage	V	208 - 575
Frequency	Hz	50 or 60

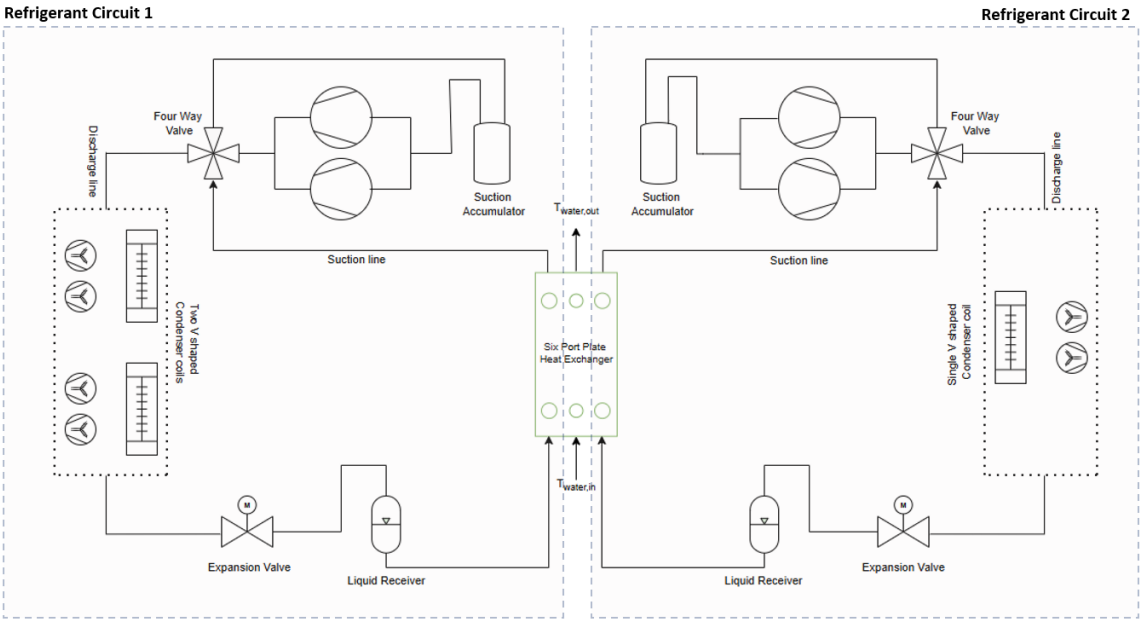


Figure 7. Piping and instrumentation diagram of the experimental test setup.

Table 3. Measurement instrumentation and specifications

Instrument	Manufacturer	Model	Accuracy
Pressure Transducers	Wika	S-10	≤ ± 0.25% of span
RTD	Pyromation	R5T185L284-006-304-19-T38	± (0.06 + 0.001 |t|) °C
Mass flow meter	ADMAG	AXF080C	±0.35% of reading

6. Results and Discussion

The steady-state numerical model and transient model was validated against cooling tests conducted at Daikin's Psychometrics Laboratory. The operating conditions for validation are summarized in Table 4. All the tests were performed in parallel flow configuration. These tests were replicated in the simulations by imposing equivalent boundary conditions for inlet specific enthalpies, pressures, and mass-flow rates, and model predictions were compared with measurements for cooling capacities of both the refrigerant circuits, with the validation results presented in the following sections having been calculated with refrigerant-side measurements. Additionally, the energy balance between the refrigerant and water sides closed to within approximately 6–8%.

Table 4. Test conditions performed and used for validation.

Input Parameters	Test 1	Test 2	Test 3	Test 4	Test 5	Test 6	Test 7
Water Circuit							
inlet temperature (°C)	12.2	11.5	10.5	12.5	12.5	12.5	12.5
mass flow rate (kg/s)	15.03	15.04	15.04	14.63	14.63	14.63	14.63
Refrigerant Circuit 1							
inlet pressure (bar)	8.58	8.42	8.65	8.68	8.65	8.66	8.67
inlet specific enthalpy (kJ/kg)	281.4	263.5	248.0	282.0	282.8	283.7	284.9
mass flow rate (kg/s)	1.02	1.02	0.54	1.03	1.04	1.02	1.02
Refrigerant Circuit 2							
inlet pressure (bar)	9.14	9.36	8.65	9.10	9.2	9.21	9.23
inlet specific enthalpy (kJ/kg)	278.5	264.4	9.12	278.8	280.0	280.5	281.4
mass flow rate (kg/s)	0.52	0.234	0.23	0.52	0.52	0.52	0.52

6.1. Experimental validation of the steady state numerical model

The steady-state numerical model exhibited excellent agreement with experimental measurements, confirming its reliability in predicting the thermal performance of the dual-circuit system. As shown in Figure 8(a), the simulated cooling capacities for both refrigerant circuits largely agree with the experimental values within ±10 %. The mean absolute error (MAE) for cooling capacity was 8.48 % for Refrigerant circuit 1 and only 0.57 % for Refrigerant circuit 2, indicating high predictive accuracy across the range of operating conditions. Similarly, the comparison of simulated and experimental total cooling capacity in Figure 8(b) shows good agreement with the experimental data, with and an overall MAE of 6.01 %. These results confirm that the implemented heat-transfer and thermodynamic models accurately capture the refrigerant-side and secondary-side interactions under steady-state operation. The close correspondence between simulation and measurement validates the robustness of the model, supporting its application for detailed performance analysis and design optimization of multi-circuit heat pump systems.

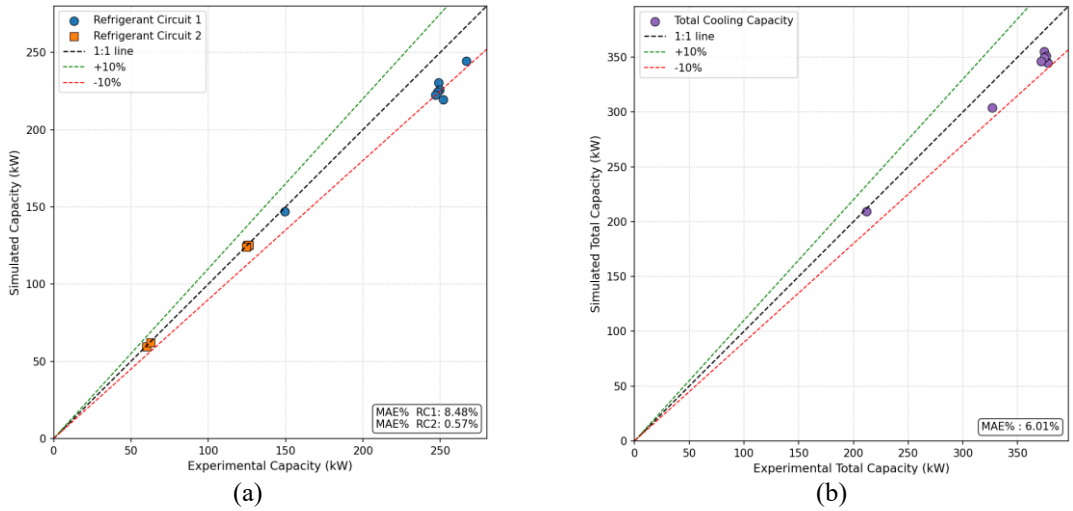


Figure 8. (a) Experimental vs simulated cooling capacity per circuit and (b) Experimental vs simulated total cooling capacity.

One of the key strengths of the finite discretized modelling approach is its ability to capture detailed temperature, HTC and vapor quality along the length of the PHE. Figure 9 illustrates the axial variation of these quantities for test condition 4, with all fluids flowing from left to right (x = 0 to 0.525 m). Both refrigerant streams enter the PHE in the two-phase region and absorb heat along the flow path. The refrigerant in circuit 2 reaches the saturation dome at a length of approximately 0.32 m and transitions into the superheated region downstream, whereas refrigerant in circuit 1 remains in the two-phase regime throughout the length of the PHE. This behaviour is strongly influenced by the imposed mass flow rates. Circuit 1 operates at a higher refrigerant mass flow rate and therefore carries a larger fraction of the total thermal load, requiring a longer effective length to approach complete evaporation.

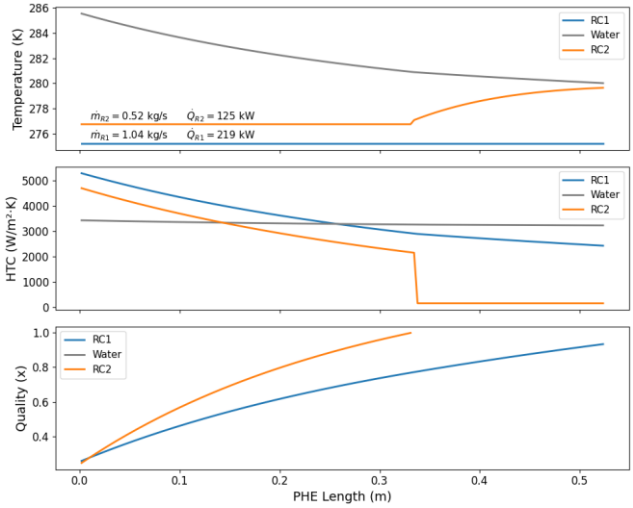
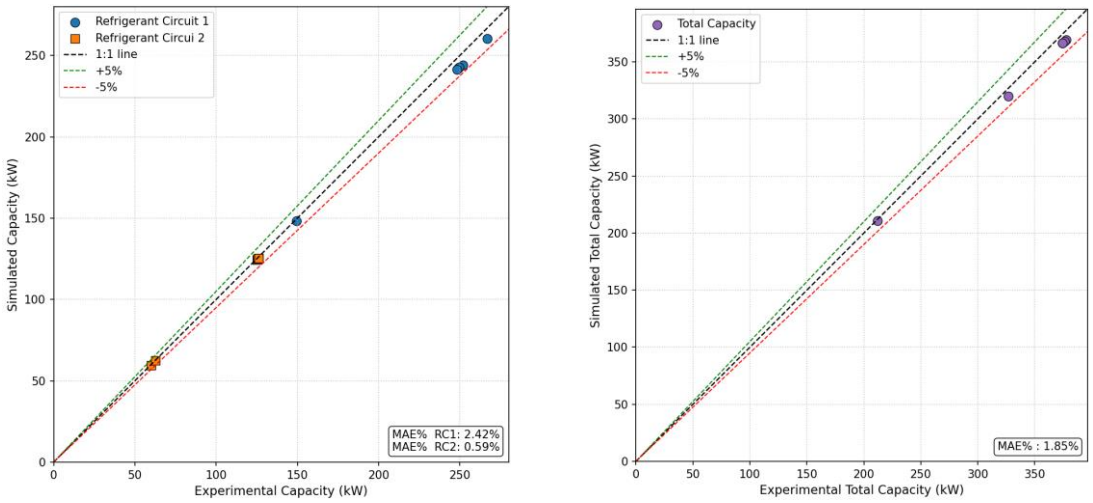


Figure 9. Temperature, heat transfer coefficient and vapor quality profiles along the length of a parallel flow six-port PHE

As seen in refrigerant circuit 2, the refrigerant-side HTC under two-phase conditions decreases progressively along the flow direction, consistent with the reduction in local heat flux as the local temperature difference diminishes. Once the refrigerant exits the saturation region, the HTC drops sharply as heat transfer transitions to single-phase vapor convection. When refrigerant circuit 2 enters the superheated region and its HTC deteriorates, its contribution to the total heat transfer decreases, while refrigerant circuit 1 continues to absorb heat under two-phase conditions. Collectively, these spatially resolved profiles provide insight into regions of high heat transfer effectiveness, performance degradation, and circuit-level imbalance information that is critical for optimizing plate length, balancing refrigerant distribution, and guiding control strategies in multi-circuit and multi-fluid PHE applications.

6.2. Experimental validation of the transient model

To ensure that the transient model operates consistently and that the implemented heat transfer and thermodynamic sub models are physically accurate, the model was evaluated under steady-state conditions. The tests from Table 2 are validated in the transient model. Figure 10(a) compares the experimental and simulated cooling capacities for both refrigerant circuits, showing a higher accuracy behavior with MAEs of 2.42% for Refrigerant circuit 1 and 0.59% for Refrigerant circuit 2. Similarly, Figure 10(b) compares the simulated and measured total cooling capacity of the PHE, with total cooling capacity deviations confined within ±1.85%. These results confirm that the transient model accurately reproduces steady-state performance, ensuring that the heat distribution between both refrigerant circuits remains thermodynamically consistent and accurately governed by the implemented heat transfer mechanisms. This provides confidence that the model can be extended to study dynamic operating scenarios in multi-circuit HPs, where time-dependent interactions and source fluctuations become significant. The testing conducted in the third-party laboratory focused exclusively on steady state characterization. As a result, the transient model validation presented here validates the underlying physics and numerical consistency of the dynamic formulation at steady state conditions rather than providing full experimental validation with time resolved data. Comprehensive transient experiments incorporating time dependent flow redistribution and valve actuation effects for model validation are planned for future phases of this research.



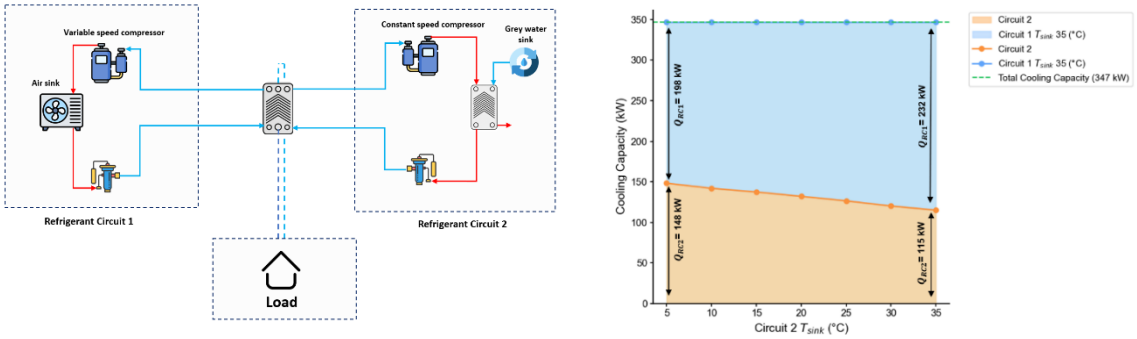
(a) (b)

Figure 10. (a) Experimental vs simulated cooling capacity per circuit and (b) Experimental vs simulated total cooling capacity.

6.3 Example analysis of efficiency improvement using six port PHE in a dual circuit heat pump.

Figure 11 illustrates how a six-port PHE can improve system efficiency by reallocating the cooling load based on the availability of lower sink temperatures. In this example analysis as shown in Figure 11(a), Refrigerant circuit 1 uses air as the sink using variable-speed compressor (higher capacity) and Refrigerant circuit 2 uses constant speed compressor (relatively lower capacity) rejects heat to a variable temperature sink, such as greywater in a multi-family residential building. As shown in Figure 11(b), for a required cooling load of 347 kW, when both circuits operate at a sink temperature of 35 °C, the load is met by the combined system. However, if Refrigerant circuit 2 encounters a lower-temperature sink, its cooling capacity increases, reducing

the burden on the air-source circuit which operates at higher constant T_{sink}. The variable-speed compressor in Refrigerant circuit 1 then adjusts its speed to supply only the remaining portion of the load. This example demonstrates that a portion of the required cooling can preferentially reject heat to lower-temperature sinks instead of relying predominantly on a higher-temperature air sink, thereby improving overall system efficiency and enhancing the operational adaptability of the integrated HP configuration. The developed modeling framework can therefore support the design of more efficient MSHP systems that maximize the use of low-exergy thermal resources, contributing to reduced energy consumption and enabling broader decarbonization of building heating and cooling applications.



(a) (b)

Figure 11: (a) Example scenario of a dual circuit HP employing a six port PHE to enable load sharing between air and grey water as sink (b) Cooling capacity redistribution in a dual circuit HP using a six port PHE to enhance efficiency under varying sink temperatures

7. Conclusion

A detailed finite-volume steady-state and transient numerical model of a six-port plate heat exchanger was developed and validated against experimental data obtained from Daikin's Psychrometrics Laboratory. The validation results demonstrated strong agreement between the simulated and measured performance, confirming the accuracy and physical consistency of both modeling frameworks. Furthermore, the transient model provides a powerful platform to investigate dynamic operating scenarios, including time-dependent load variations, source fluctuations, and control responses. The validated framework can be seamlessly integrated into multi-circuit heat pump systems to analyze coupled refrigerant–water interactions, circuit-level heat distribution, and overall thermal performance

8. Nomenclature

p	pressure (kPa)	Pr	Prandtl number (-)
T	temperature (K)	V	molar volume ($m^3 \cdot mol^{-1}$)
h	specific enthalpy $(J.kg^{-1})$	t	time (s)
η	dynamic viscosity of the bulk fluid (Pa·s)	η_w	dynamic viscosity at the wall temperature (Pa·s)
H_g	Hagen number (-)	c_q , q	0.122, 0.374
k	fluid thermal conductivity ($W \cdot m^{-1} \cdot K^{-1}$)	d_h	hydraulic diameter (m)
p^*	reduced pressure (-)	rp	surface roughness (μm)
q	Heat flux ($W \cdot m^{-2}$)	M	Molecular weight ($kg \cdot mol^{-1}$)
α	Heat transfer coefficient ($W \cdot m^{-2} \cdot K^{-1}$)	ρ	fluid density ($kg \cdot m^{-3}$)
$\dot{Q}$	Heat transfer rate (W)	ξ	mass fraction (-)
β	Volumetric thermal coefficient of expansion (K^{-1})	v	volume (m^3)

Acknowledgements

We gratefully thank Daikin Applied for sponsoring this project, providing technical guidance and for their experimental validation support in their Psychrometrics Laboratory.

References

[1] International Energy Agency. The Future of Heat Pumps. Available at: https://www.iea.org/reports/the-future-of-heat-pumps. Accessed 2025.
[2] Milev G., Al-Habaibeh A., Fanshawe S., Luke Siena F., 2023. Investigating the effect of the defrost cycles of air-source heat pumps on their electricity demand in buildings. Energy and Buildings 300, p. 113656.
[3] Klingebiel J., Höges C., Göbel S., Bannmüller P., Boelsen T., Venzik V., Vering C., Müller D., 2025. Optimal defrost initiation for air-source heat pumps: Evaluating the improvement potential of common defrosting controllers. Energy 324, p. 135871.
[4] Natale C., Dongellini M., Naldi C., Morini G.L., 2025. Evaluation of the seasonal energy performance of a dual-source heat pump through dynamic experimental tests. Energies 18(10), p. 2532.
[5] Adebayo P., Shor R., Mohamad A.A., Wemhöner C., Mwesigye A., 2024. Performance analysis of a solar-assisted ground source heat pump with a single vertical U-tube ground heat exchanger. Applied Thermal Engineering 257, p. 124452.
[6] Nouri G., Noorollahi Y., Yousefi H., 2019. Solar assisted ground source heat pump systems – A review. Applied Thermal Engineering 163, p. 114351.
[7] SWEP. "6.8 Brazed plate heat exchanger evaporators," SWEP Refrigeration Handbook, SWEP, Accessed Aug. 22 2025.
[8] Stenhede C., 2004. Plate Heat Exchangers for Refrigeration Applications: Technical Reference Manual, 5th ed., Lund, Sweden: Alfa Laval AB
[9] D. P. Sekulić, "Thermal design theory of three-fluid heat exchangers," in *Advances in Heat Transfer*, J. P. Hartnett and T. F. Irvine, Eds., vol. 26, Elsevier, 1995
[10] J. A. W. Gut and J. M. Pinto, "Modeling of plate heat exchangers with generalized configurations," *International Journal of Heat and Mass Transfer*, vol. 46, no. 14, pp. 2571–2585, 2003
[11] G. Skaugen, K. Kolsaker, H. T. Walnum, and Ø. Wilhelmsen, "A flexible and robust modelling framework for multi-stream heat exchangers," *Computers & Chemical Engineering*, vol. 49, pp. 95–104, 2013
[12] Qiao H., Aute V., Lee H., Saleh K., Radermacher R., 2013. A new model for plate heat exchangers with generalized flow configurations and phase change. International Journal of Refrigeration 36(2), pp. 622–632.
[13] TLK-Thermo GmbH. TIL Suite – Libraries for Technical Thermodynamics in Modelica, Braunschweig, Germany.
[14] Martin H., 2010. VDI Heat Atlas, Chapter B6: Pressure Drop and Heat Transfer in Plate Heat Exchangers, VDI-Verlag, Düsseldorf.
[15] Eldeeb R., Aute V., Radermacher R., 2016. A survey of correlations for heat transfer and pressure drop for evaporation and condensation in plate heat exchangers. International Journal of Refrigeration 65, pp. 12–26.
[16] Palm, B., Claesson, J., 2006. Plate heat exchangers: calculation methods for single- and two-phase flow. *Heat Transfer Engineering* **27**(4), 88–98.
[17] Cooper M.G., 1984. Heat flow rates in saturated nucleate pool boiling – A wide-ranging examination using reduced properties. In: Hartnett J.P., Irvine T.F. Jr. (eds.) Advances in Heat Transfer, vol. 16, Academic Press, Orlando, FL, pp. 157–239.
[18] Petzold R., 1982. A description of DASSL: A Differential/Algebraic System Solver. Sandia National Laboratories Report, Albuquerque, USA